

Chapter 7

J/ Ψ Transverse Spin Dependent Analysis

This chapter describes the analysis performed in the intermediate invariant mass range at COMPASS. The biggest advantage about the intermediate mass range is an increase in statistics. The intermediate mass range contains approximately 1.6 times more events than the high mass range above 4.3 GeV/ c^2 . On the other hand, the intermediate mass range results from several reactions. Never the less, J/ Ψ production is by far the most dominate reaction and therefore the this chapter assumes the results are from the J/ Ψ reaction. A theoretical introduction related to transverse J/ Ψ spin asymmetries is provided in Sec 2.5.4. As of yet, the exact mechanism for J/ Ψ production is unknown and therefore the exact J/ Ψ vertex coupling is unknown. Never the less, the analysis techniques in this chapter contribute to the transverse spin knowledge resulting from J/ Ψ production. The reaction of interest is

$$\pi^-(P_a) + P(P_b, S_T) \rightarrow J/\Psi + X \rightarrow \mu^-(\ell) + \mu^+(\ell') + X, \quad (7.1)$$

where the proton target, P , is transversely polarized with spin S_T .

The dimuon final state from J/ Ψ production is indistinguishable from the Drell-Yan dimuon final state described the previous analyses in chapter 6. For this reason, similar event selection and data quality are used to study the dimuon production resulting from J/ Ψ decays. On the other hand, the J/ Ψ production has a higher background percentage from Drell-Yan and other components to be taken into account. The results presented in this chapter are determined from the left-right asymmetry analysis as in Sec 6.5, where again the left-right asymmetry is defined as

$$A_{lr} = \frac{1}{|S_T|} \frac{\sigma_l - \sigma_r}{\sigma_l + \sigma_r}. \quad (7.2)$$

7.0.1 Data Collection and Event Selection

The data collection is described in Sec 6.1.1 and the data stability tests are described in Sec 6.1.2. Both the Drell-Yan analysis and the J/ Ψ production analysis study dimuon final states so the spectrometer data

taking conditions are the same. In particular the measurement in this chapter results from a 190 GeV/c π^- beam impinged on a transversely polarized NH_3 target from the 2015 COMPASS spectrometer data taking conditions.

The event selection in this chapter is similar to the event selection in the previous chapter, Sec 6.1.3. The cuts are chosen to ensure two oppositely polarized muons are detected with a vertex in the transversely polarized NH_3 target. Table 6.1.3 describes the cut selection and the reason from each cut. The only event selection difference, from Table 6.1.3, is the selected invariant mass. The nominal J/Ψ invariant mass and width are 3.096 GeV/ c^2 and 92.9×10^{-6} GeV/ c^2 respectively [1]. Therefore to ensure the events for this analysis result from J/Ψ production, the analysis invariant mass range should be where the J/Ψ signal to background is highest. This is in contrast to the Drell-Yan analyses which required the invariant mass to be above 4.3 GeV/ c^2 .

J/Ψ Invariant Mass Range

The COMPASS spectrometer has a finite mass resolution which therefore means the events resulting from J/Ψ production have an invariant mass spread larger than the nominal J/Ψ width. For this reason the cut on invariant mass should be a range much larger than the nominal J/Ψ width. Fig. 7.1 shows the 2015 dimuon invariant mass distribution and the other production components around the J/Ψ invariant mass.

As can be seen in Fig. 7.1 regardless of the analysis mass range chosen, there are still events resulting from the other background processes. The normalized systematic variance resulting from background processes is derived in Appendix A.3 as

$$\frac{\sigma_{\text{systematic}}^2}{\sigma_{\text{statistical}}^2} = \frac{(1-p)^2}{p^2}, \quad (7.3)$$

and the total variance from statistical fluctuations and background contributions is

$$\delta^2 A_{lr, \text{J}/\Psi} = \frac{(1-p)^2 + 1}{p^2} \sigma_{\text{statistical}}^2, \quad (7.4)$$

where p is the J/Ψ purity. Therefore the analysis invariant mass range should have a J/Ψ purity as high as possible to reduce the systematic error while still including as much data as possible to reduce the statistical error. The total error however, is dominated by statistical error for any purity larger than 50%. That being the case, Eq. 7.4 is derived assuming $(1-p)$ is small and therefore a desired purity of 90% or greater was chosen to safely ensure Eq. 7.4 is valid.

The J/Ψ purity as a function of mass range is determined from a Monte-Carlo data set. The same Monte-

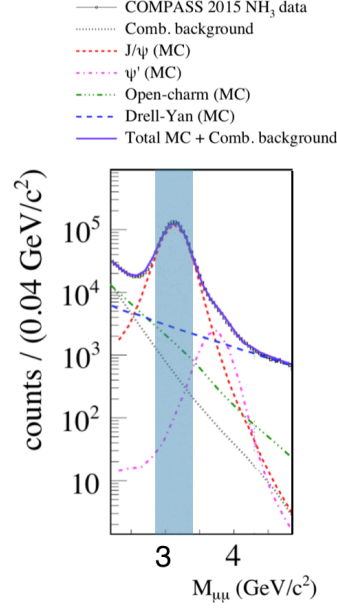


Figure 7.1: The 2015 COMPASS invariant dimuon mass distribution and a fit to this data. The data fit is from Monte-Carlo and combinatorial background analysis and is provided to show the background processes. The shaded blue region shows the analysis mass range for the analysis in this chapter. This image is taken from [18].

Carlo described in Table 6.7 was used to calculate the J/Ψ purity. In particular the processes included are Drell-Yan production, open charm production, Ψ' production and J/Ψ production. To determine the purity, the real data is fit using the Monte-Carlo data which determines the counts from each process. The Monte-Carlo fit is accomplished by normalizing the invariant mass distribution from each Monte-Carlo sample and then fitting using the sum of the four normalized distributions to fit the real data. The fit function is defined as

$$F_{J/\Psi \text{ Fit}}(x) = N_{J/\Psi} h_{J/\Psi}(x) + N_{Drell-Yan} h_{Drell-Yan}(x) + N_{Open \text{ Charm}} h_{Open \text{ Charm}}(x) + N_{\Psi'} h_{\Psi'}(x), \quad (7.5)$$

where $h(x)$ represents the number of counts from the normalized histogram distribution and the N 's are the fit parameters. Fig. 7.2 shows the four normalized Monte-Carlo invariant mass distributions and Fig. 7.3 shows the Monte-Carlo fit to the real data in one q_T bin.

Once the fits are performed, the J/Ψ purity in each invariant bin is determined as

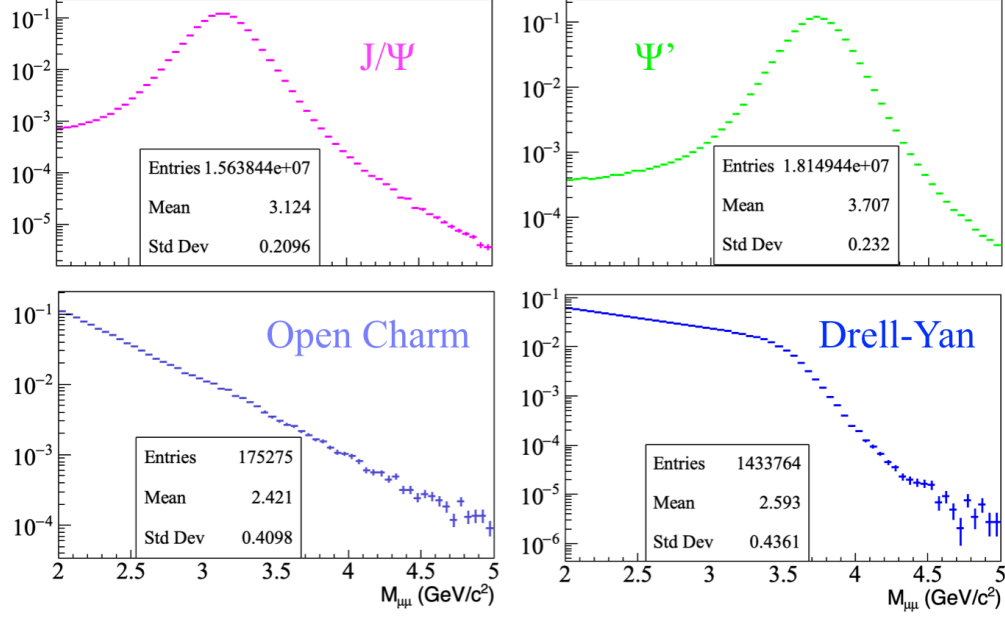


Figure 7.2: The normalized invariant mass distributions from the four simulated Monte-Carlo processes. These distributions are used to fit the real data.

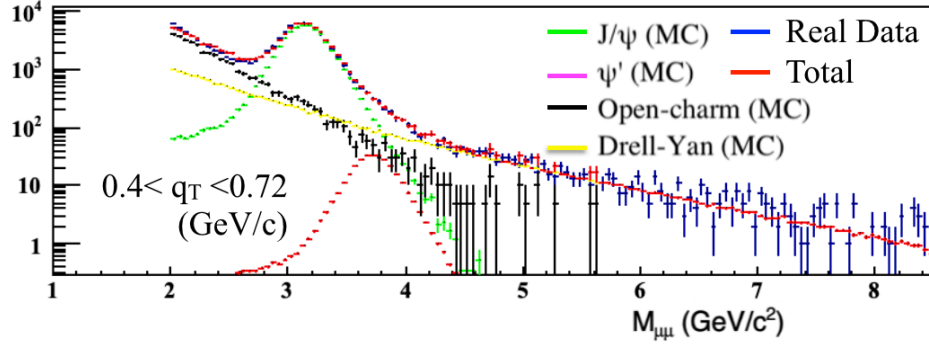


Figure 7.3: An example of the Monte-Carlo fit to real data in one q_T bin of the real data. This fit is used to determine the distribution of J/Ψ purity.

$$p(x) = \frac{N_{J/\Psi} h_{J/\Psi}(x)}{N_{J/\Psi} h_{J/\Psi}(x) + N_{Drell-Yan} h_{Drell-Yan}(x) + N_{Open\ Charm} h_{Open\ Charm}(x) + N_{\Psi'} h_{\Psi'}(x)}. \quad (7.6)$$

Table 7.1 summarizes the J/Ψ purity as a function of the mass range. For this analysis an invariant mass range of 2.87-3.38 GeV/ c^2 was chosen to safely have a J/Ψ purity of 90% or greater. Tables 7.2- 7.3 summarizes the number of events remaining after each cut.

Mass range GeV/c ²	J/Ψ Purity %
2.5-4.3	79.7 ± 2.9
2.78-3.46	88.9 ± 2.0
2.87-3.38	91.3 ± 1.5
2.95-3.29	92.9 ± 1.0
3.08-3.17	94.0 ± 1.0

Table 7.1: J/Ψ purity as a function of the invariant mass range

Cuts	W07	W08	W09	W10	W11
$\mu^- \mu^+$ 2-8.5 GeV/c ² with a common best primary vertex	1,573,372	1,572,255	1,620,593	1,683,263	2,598,485
Good Spills	1,298,306	1,223,877	1,333,335	1,374,620	1,901,071
$0 < x_\pi \ x_N < 1, -1 < x_F < 1$	1,298,278	1,223,851	1,333,307	1,374,599	1,901,033
$0.4 < q_T < 5(\text{GeV}/c)$	1,121,908	1,056,835	1,151,253	1,187,125	1,641,463
Z Vertex within NH ₃	314,965	298,531	324,413	335,659	465,172
Vertex Radius < 1.9cm	308,278	292,114	317,985	328,658	455,580
$2.87 < M_{\mu\mu} < 3.38 (\text{GeV}/c^2)$	170,041	160,450	174,696	180,795	250,921

Table 7.2: Selected dimuon events for the first five data periods from the intermediate mass range analysis of 2015 COMPASS data

Cuts	W12	W13	W14	W15	W11	Remaining
$\mu^- \mu^+$ 2-8.5 GeV/c ² with a common best primary vertex	1,932,425	1,680,706	1,094,525	640,095	14,395,719	100.00 %
Good Spills	1,659,030	1,314,489	982,131	616,734	11,703,593	81.3 %
$0 < x_\pi \ x_N < 1, -1 < x_F < 1$	1,658,996	1,314,470	982,125	616,720	11,703,379	81.3 %
$0.4 < q_T < 5(\text{GeV}/c)$	1,432,115	1,134,223	846,897	532,045	10,103,864	70.2 %
Z Vertex within NH ₃	406,975	322,964	241,673	151,937	2,862,289	19.9 %
Vertex Radius < 1.9cm	398,610	316,149	236,019	148,834	2,802,227	19.5 %
$2.87 < M_{\mu\mu} < 3.38 (\text{GeV}/c^2)$	219,110	173,701	129,346	81,808	1,540,868	10.7 %

Table 7.3: Selected dimuon events for the last four data periods and the total number of events from the intermediate mass range analysis of 2015 COMPASS data

7.0.2 Binning

The analysis is determined as a function of the variables x_N , x_π , x_F , q_T and $M_{\mu\mu}$. These are the same variables used to bin the high mass Drell-Yan analysis. The left-right asymmetry analysis is binned in each of the kinematic variables by requiring an equal amount of data per kinematic bin. The bin limits are also required to have a width of at least three times the resolution per variable. For this analysis there are enough events and the resolution per variable is good enough to have four kinematic bins. The bin limits are provided in Table [7.5](#) and the spectrometer resolutions are provided in Table [7.4](#).

The spectrometer resolution is determined from the Monte-Carlo data. The resolution is determined from the difference between the Monte-Carlo generated value and the reconstruction Monte-Carlo value. An

example of this distribution is shown in Fig. 7.4 for the x_π variable. The distribution has a longer tail than a Gaussian distribution and for this reason a two Gaussian fit function is used to determine the distribution's width. The resolution is then determined as the width of the Gaussian with the larger amplitude, so-called leading order Gaussian. The actual spectrometer resolution is between the width of the leading order Gaussian and the RMS of the distribution. However the leading order Gaussian width is closer to the true resolution and is therefore used as the estimate for the spectrometer resolution.

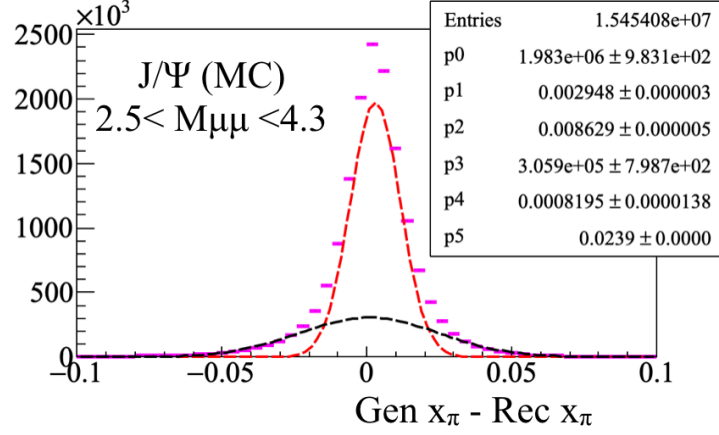


Figure 7.4: The distribution of generated x_N minus reconstructed x_N . The leading Gaussian width (red) is used to determine the resolution.

Variable	RMS	Leading Gaussian σ
x_N	0.01	0.006
x_π	0.0157	0.009
x_F	0.016	0.011
q_T	0.143	0.022

Table 7.4: COMPASS spectrometer resolutions in the intermediate mass range 2.5-4.3GeV/ c^2

Variable	Lowest limit	Upper limit bin 1	Upper limit bin 2	Upper limit bin 3	Upper limit bin 4
x_N	0.0	0.062	0.083	0.11	1.0
x_π	0.0	0.21	0.28	0.38	1.0
x_F	-1.0	0.10	0.20	0.32	1.0
q_T (GeV/c)	0.4	0.72	1.04	1.47	5.0
$M_{\mu\mu}$ (GeV/ c^2)	2.87	3.03	3.13	3.22	3.38

Table 7.5: The J/ Ψ analysis bin limits for the four analysis bins

The distributions for the binning variables are shown in Fig. 7.5. This analysis is performed in the valence region for both the beam pion and target proton as the average x_π is about 0.09 and the average x_N is about 0.3. This means the dominate contribution to J/ Ψ production is from quark-quark interactions.

The average q_T value is below the minimum mass range of 2.87 GeV/ c^2 for this analysis and therefore the interpretation of this analysis assumes the TMD regime is valid.

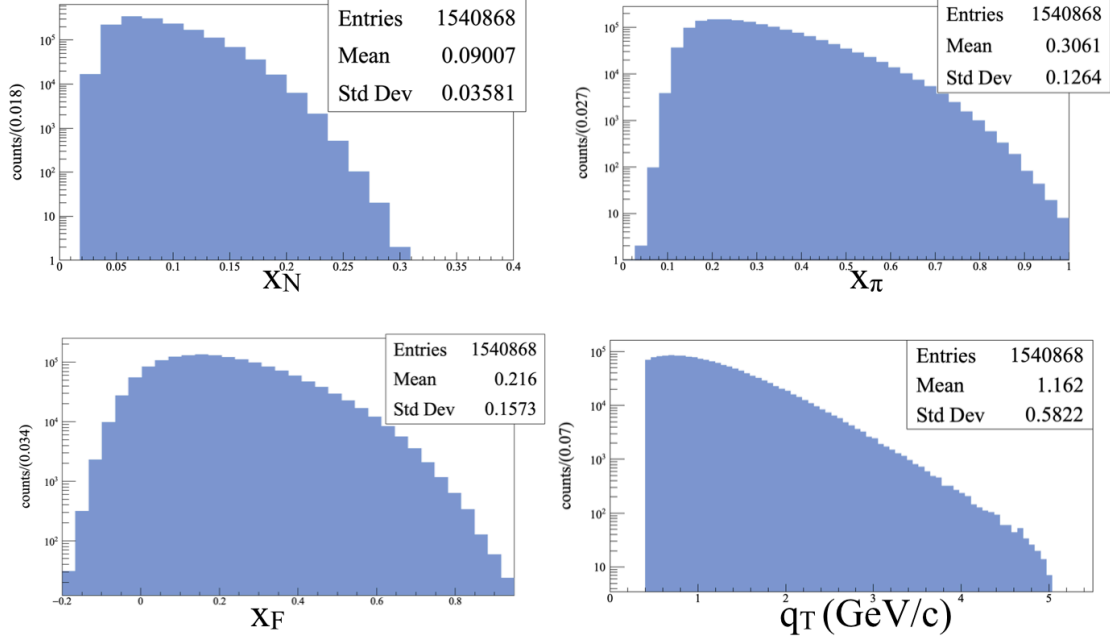


Figure 7.5: The binning variable distributions. The longitudinal momentum fractions x_N (top left) and x_π (top right) and the x_F (bottom left) and the virtual photon transverse momentum q_T (bottom right). These distributions are plotted from in the mass range 2.87-3.38 GeV/ c^2 .

7.0.3 Asymmetry Extraction

The asymmetry extraction method used is the two-target geometric mean. This asymmetry method is described in detail in Secs [6.5](#) [6.5.1](#). The asymmetry is again defined as

$$A_{lr,2Targ} = \frac{1}{|S_T|} \frac{\sqrt[4]{N_{1,l}^\uparrow N_{1,l}^\downarrow N_{2,l}^\uparrow N_{2,l}^\downarrow} - \sqrt[4]{N_{1,r}^\uparrow N_{1,r}^\downarrow N_{2,r}^\uparrow N_{2,r}^\downarrow}}{\sqrt[4]{N_{1,l}^\uparrow N_{1,l}^\downarrow N_{2,l}^\uparrow N_{2,l}^\downarrow} + \sqrt[4]{N_{1,r}^\uparrow N_{1,r}^\downarrow N_{2,r}^\uparrow N_{2,r}^\downarrow}}, \quad (7.7)$$

where N represents the counts, $l(r)$ denotes left(right), 1(2) denotes the target cell and \uparrow (\downarrow) denotes the transverse polarization direction. The definitions of left and right are defined relative to the target spin as

$$\begin{aligned} \text{Left} : \hat{q}_T \cdot (\hat{S}_T \times \hat{P}_\pi) &> 0 \\ \text{Right} : \hat{q}_T \cdot (\hat{S}_T \times \hat{P}_\pi) &< 0, \end{aligned} \quad (7.8)$$

where \hat{q}_T , \hat{S}_T and \hat{P}_π are unit vectors in the target reference frame for the virtual photon transverse momentum, the target spin and the beam pion momentum respectively. The advantage to this asymmetry method

is that the acceptance from the upstream and downstream target cells cancel as was shown in Eq. [6.26](#). The statistical uncertainty for this asymmetry method can be written as

$$\delta A_{lr,2Targ} = \frac{1}{|S_T|} \frac{LR}{(L+R)^2} \sqrt{\sum_{c,p} \left(\frac{1}{N_{c,l}^p} + \frac{1}{N_{c,r}^p} \right)} , \quad (7.9)$$

where $L = \sqrt[4]{N_{1,l}^\uparrow N_{1,l}^\downarrow N_{2,l}^\uparrow N_{2,l}^\downarrow}$ and $R = \sqrt[4]{N_{1,r}^\uparrow N_{1,r}^\downarrow N_{2,r}^\uparrow N_{2,r}^\downarrow}$. In the approximate case of equal statistical populations in each left-right direction and each target cell, the statistical uncertainty for the two-target geometric mean reduces to $\frac{1}{|S_T|} \frac{1}{\sqrt{N}}$, where N is the sum of all counts.

7.0.4 Systematic Studies

Similar tests as were performed for the high mass left-right asymmetry to determine the systematic error are also performed for the intermediate mass left-right asymmetry. For the full details on the previous tests see Sec [6.5.2](#). This section will give the results for systematic errors in the intermediate mass range and describe in detail the tests specific to this analysis. The overall systematic errors are determined by adding all non-zero systematic uncertainties in quadrature. The impact from each source of systematic error is summarized in Table. [7.7](#)

Period Compatibility (Time Dependence)

It is expected that the asymmetry calculation will vary in time due to statistical fluctuations. Fig. [7.6](#) shows the left-right asymmetry calculated for each period in time and Fig. [7.7](#) shows the left-right asymmetry time fluctuations for each bin in x_N . To quantify if the time fluctuations are greater than what is expected from random statistical fluctuations, the pull distribution is checked for a larger width than one or a non-zero mean. More details on the pull distribution are given in Sec [6.5.2](#).

The pull value is defined as

$$\Delta A_i = \frac{A_i - \langle A \rangle}{\sqrt{\sigma_{A_i}^2 - \sigma_{\langle A \rangle}^2}}. \quad (7.10)$$

The pull distribution is formed for each kinematic variable in Fig. [7.8](#). For this analysis there are therefore 4 (number of bins) \times 9 (number of periods) = 36 entries per pull distribution. The systematic error from period incompatibility is determined as

$$\frac{\sigma_{systematic}}{\sigma_{statistical}} = \sqrt{|\sigma_{pull}^2 - 1|} + \frac{\mu_{pull}}{2}, \quad (7.11)$$

where in this analysis the σ_{pull}^2 and μ_{pull} are determined as a weighted average of the mean and variance from

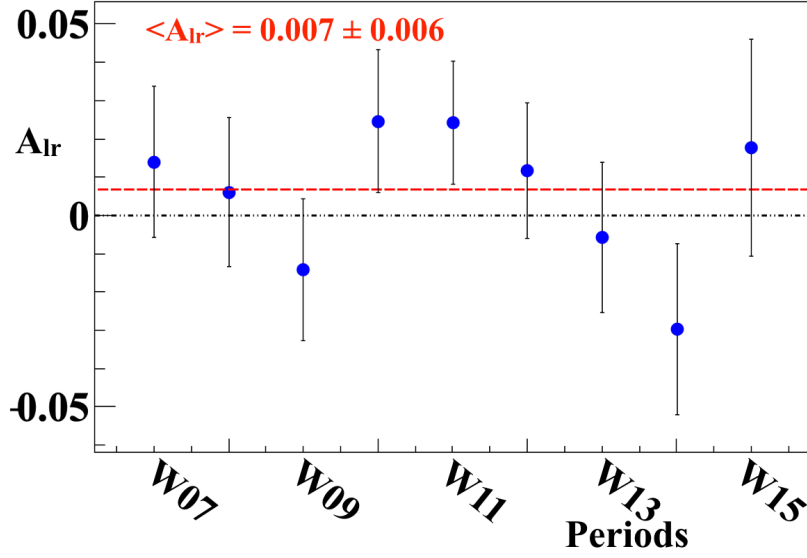


Figure 7.6: The left-right asymmetry in the J/Ψ mass region as a function of time. The red line is a constant fit and therefore shows the weighted averaged of the periods.

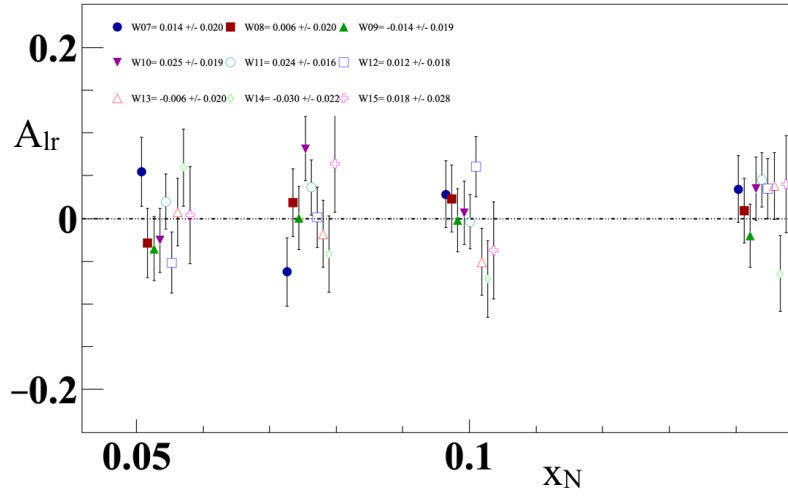


Figure 7.7: The left-right asymmetry time fluctuations in each bin of x_N .

the pull distribution for each kinematic variable including the parameters from integrated pull distribution. The fit values from each pull distribution give somewhat different estimates due to the errors associated with the fit. This is the reason the weighted average is performed to give the best estimate for the pull mean and standard deviation and therefore the most accurate systematic error calculation. The systematic error due to time incompatibility is determined to be 16% of the statistical error.

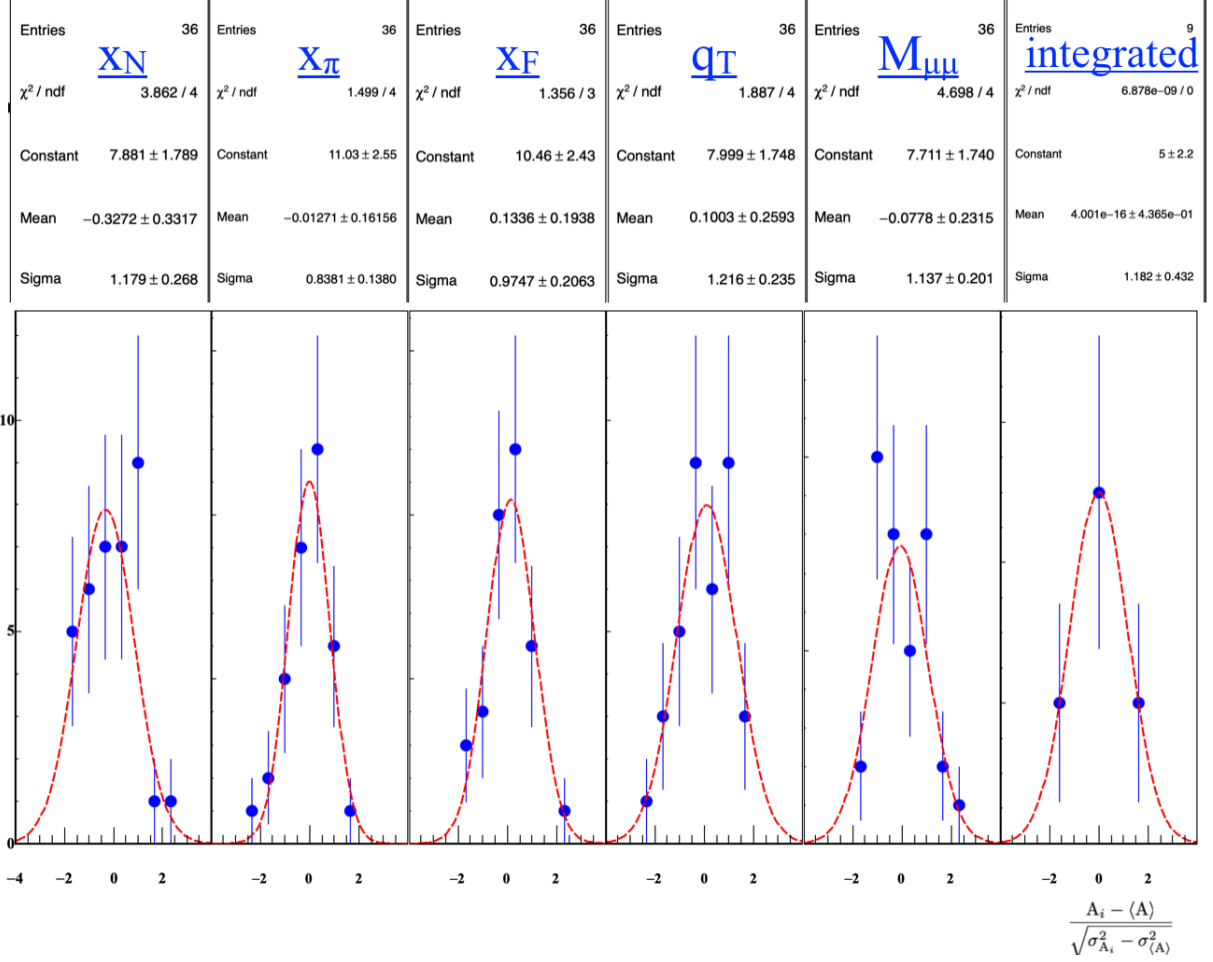


Figure 7.8: The uncorrelated pull distributions for each of the kinematical variables and a pull distribution from the integrated asymmetry from each time period.

Left/Right Event Migration

The left-right event migration systematic error is calculation the same as in Sec 6.5.2. The Monte-Carlo data used to determine the left-right event migration is described in Table 6.7. The effect of misidentify events as left when the event should be counted as a right event and vise-versa is to dilute the left-right asymmetry. It is as if there is an additional unpolarized contribution that dilutes the event sample.

The systematic error for left-right migration is derived in Appendix A.2 as

$$\delta A_{lr,systematic} = \gamma * A_{lr} + \gamma * \delta A_{lr}, \quad (7.12)$$

where γ is the fraction of misidentified left and right events.

As is clearly visible in Fig. 7.9, there is a band of higher misidentification rate at the border between left and right. For the J/Ψ mass region only about 3% of events were misidentified resulting in a systematic

error of 4.4% of the statistical error.

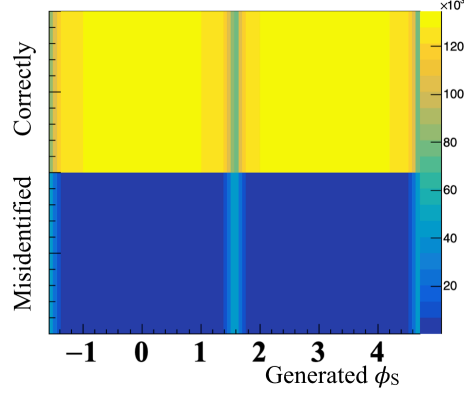


Figure 7.9: The left-right migration as a function of the generated ϕ_S angle in the mass range 2.87-3.38.

J/ Ψ Purity

The systematic error due to a J/ Ψ purity less than unity was discussed in Sec [7.0.1](#). The invariant mass range was chosen specifically such that the J/ Ψ purity is 90% or higher to reduce the systematic error associated with impurities. The systematic error is derived in Appendix [A.3](#) as

$$\frac{\sigma_{\text{systematic}}}{\sigma_{\text{statistical}}} = \frac{(1-p)}{p}. \quad (7.13)$$

Table [7.1](#) summarized the impurity as a function of the analysis mass range and the impurity in this analysis mass range is 91.3%. This corresponds to a systematic error of 9.5% of the statistical error.

False Asymmetries

Acceptance From False Asymmetries

The acceptance fluctuations are determined from the false asymmetry defined as

$$A_{lr, \text{False}} = \frac{1}{|S_T|} \frac{\sqrt[4]{N_{1,r}^\uparrow N_{1,l}^\downarrow N_{2,l}^\uparrow N_{2,r}^\downarrow} - \sqrt[4]{N_{1,l}^\uparrow N_{1,r}^\downarrow N_{2,r}^\uparrow N_{2,l}^\downarrow}}{\sqrt[4]{N_{1,r}^\uparrow N_{1,l}^\downarrow N_{2,l}^\uparrow N_{2,r}^\downarrow} + \sqrt[4]{N_{1,l}^\uparrow N_{1,r}^\downarrow N_{2,r}^\uparrow N_{2,l}^\downarrow}} = \frac{1}{|S_T|} \frac{\alpha_{2\text{Tar}g} - 1}{\alpha_{2\text{Tar}g} + 1}. \quad (7.14)$$

More details for acceptance fluctuations are discussed in Sec. [6.5.1](#) and Sec. [6.5.1](#). The kinematic dependencies of the acceptance ratio, $\alpha_{2\text{Tar}g}$, are shown in Fig. [7.10](#). As Fig. [7.10](#) shows the acceptance is only slightly greater than unity even though it can be above 1 by more than a sigma. The systematic error associated with acceptance fluctuations is defined as

$$\delta A_{lr,systematic} = \frac{1}{|S_T|} \left(\frac{|\alpha_{2Targ} - 1|}{2} + \delta_{\frac{|\alpha_{2Targ} - 1|}{2}} \right), \quad (7.15)$$

where this expression is derived in Appendix [A.1](#). The normalized kinematic dependence of the systematic error to the statistical error are shown in Fig. [7.11](#). The average systematic error due to acceptance is 23% of the statistical error.

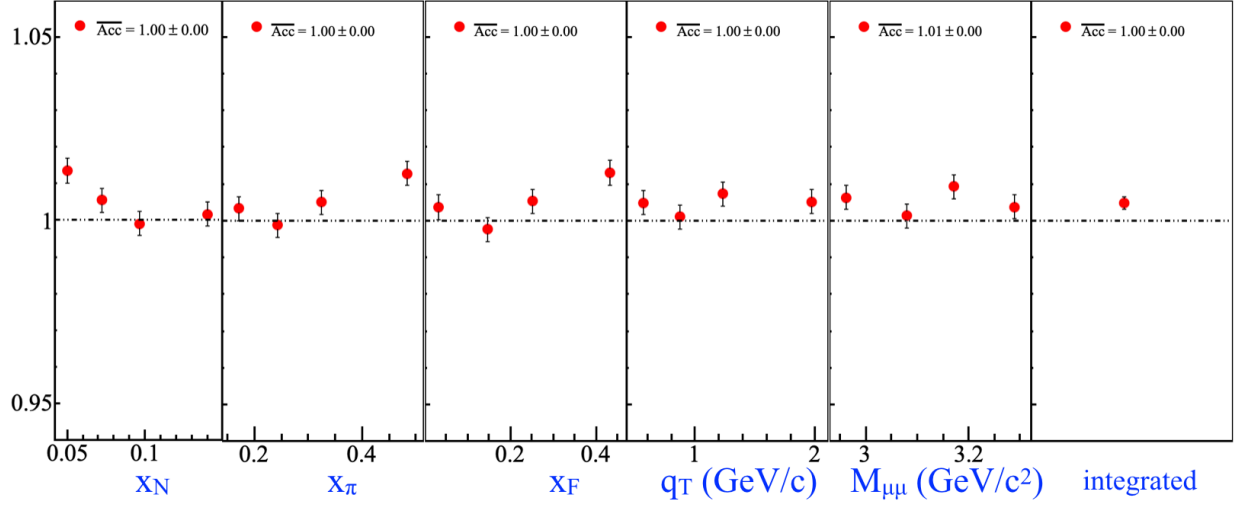


Figure 7.10: Acceptance fluctuations in each bin of the kinematic variables.

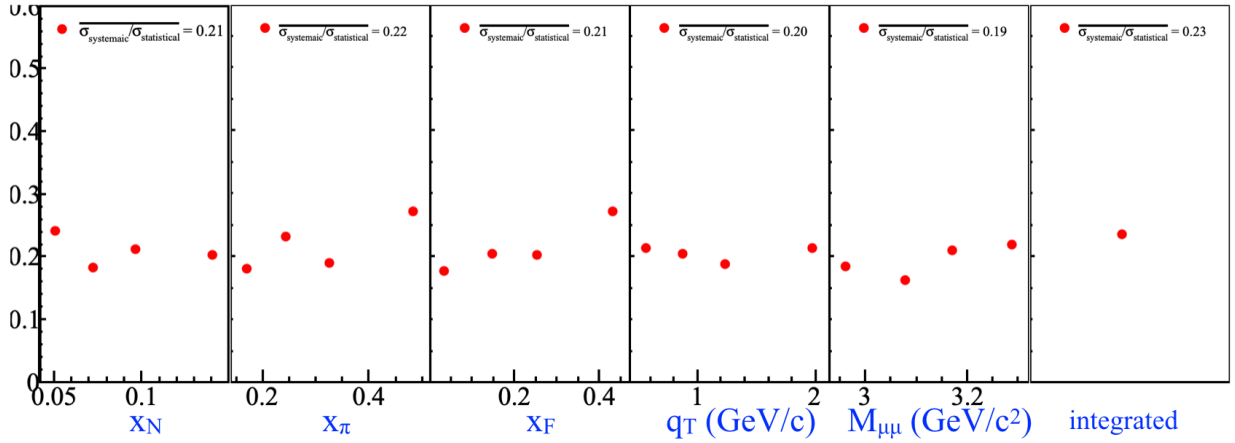


Figure 7.11: Systematic error divided by statistical error due to acceptance

Further False Asymmetry Effects

Additional false asymmetries are analyzed to account for systematic errors which were not addressed directly. The false asymmetries are constructed in such a way that the cross-section and luminosity cancel out in the numerator and the denominator. Therefore these false asymmetries can only change in time due to acceptance effects or for some unknown reason. The false asymmetries constructed to study the intermediate mass analysis are described in the following enumerated list.

1. The false asymmetry used to determine the acceptance fluctuations, Eq. 7.14 is checked for compatibility and the uncorrelated pulls are shown in Fig. 7.12 along with the corresponding fit parameters and errors.

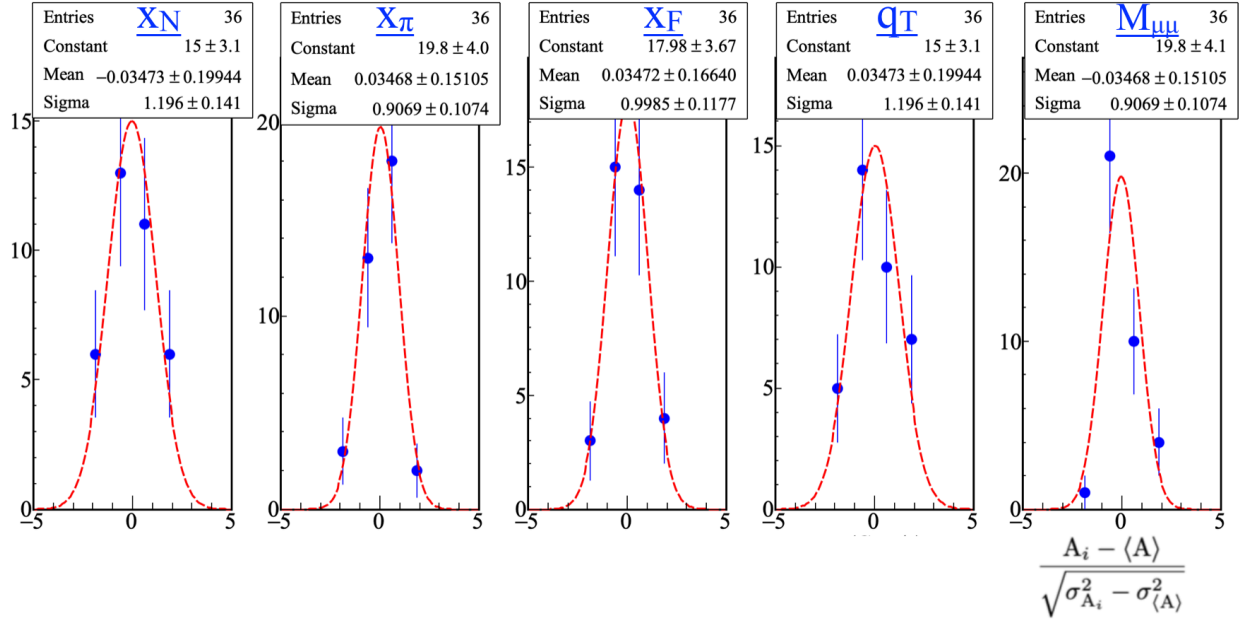


Figure 7.12: Pull distribution for a nearly acceptance free two-target false geometric mean asymmetry

2. A false asymmetries using only the information from the upstream or the downstream target cell defined as

$$A_{lr,FA} = \frac{1}{|S_T|} \frac{\sqrt{N_l^\uparrow N_r^\downarrow} - \sqrt{N_r^\uparrow N_l^\downarrow}}{\sqrt{N_l^\uparrow N_r^\downarrow} + \sqrt{N_r^\uparrow N_l^\downarrow}}. \quad (7.16)$$

The pulls for the upstream target cell are shown in Fig. 7.13 and the pulls for the downstream target cell are shown in Fig. 7.14

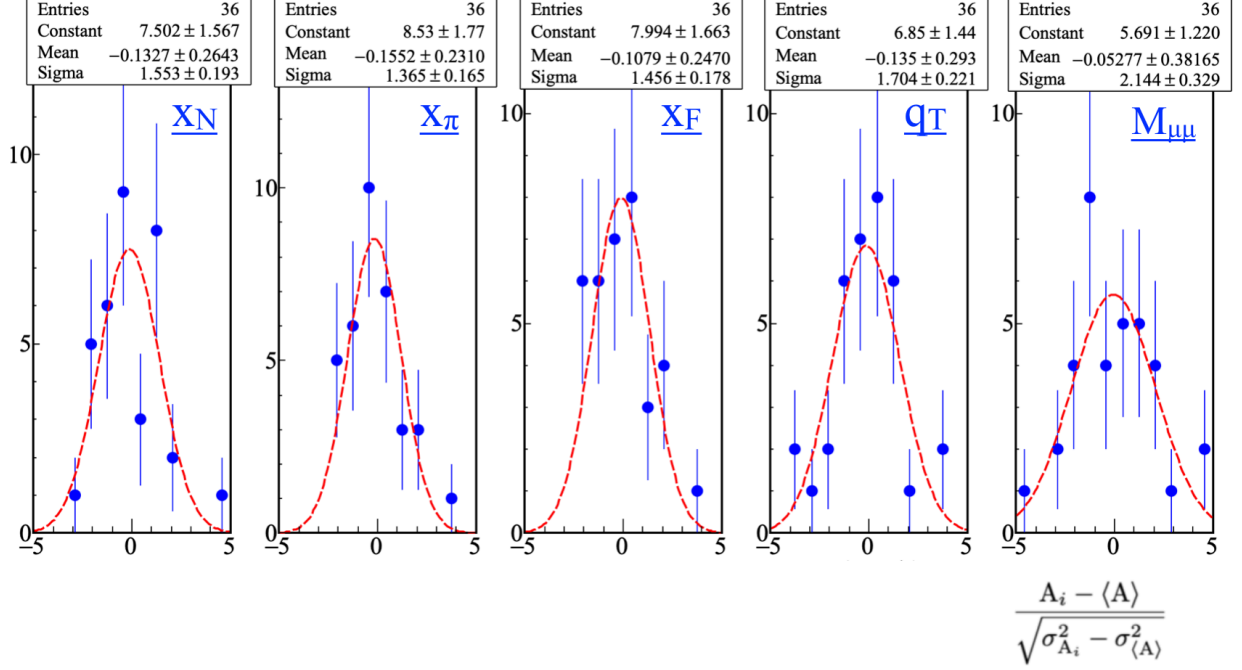


Figure 7.13: Pull distributions from the false asymmetry in the upstream target cell

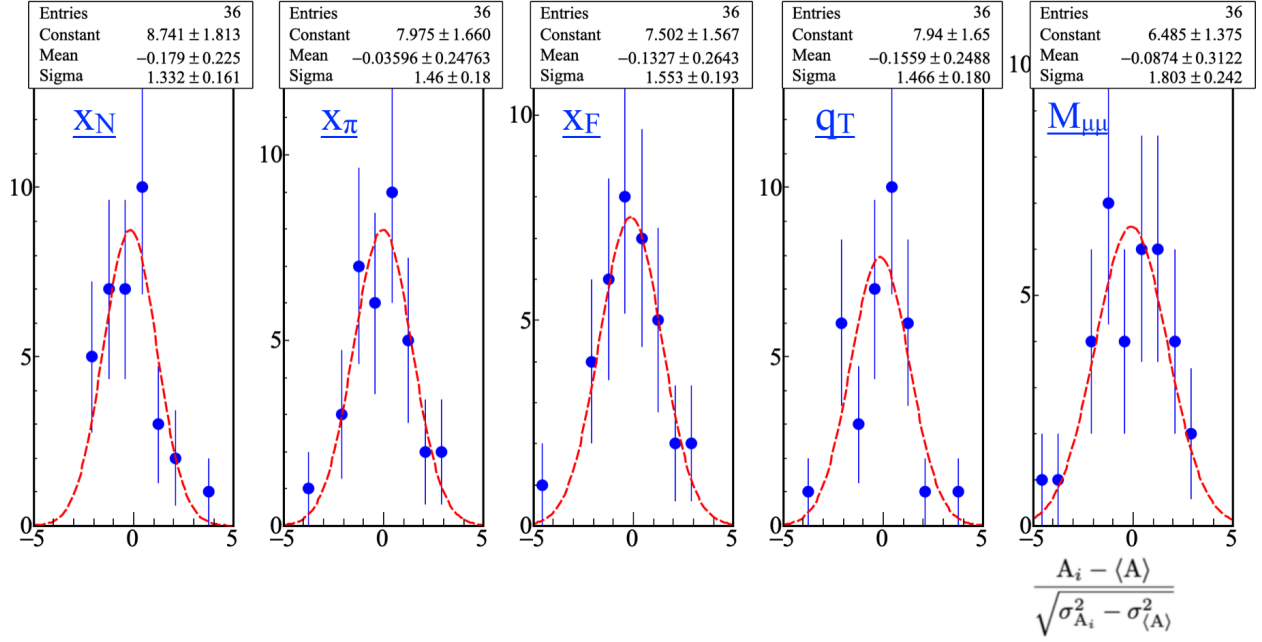


Figure 7.14: Pull distributions from the false asymmetry in the downstream target cell

The systematic error from each false asymmetry is determined using the Eq. [7.11](#). The uncorrelated pulls have only 4 (number of bins) \times 9 (number of periods) = 36 entries which results in large errors on

the Gaussian fit results. In an attempt to correct for this and to take into account the fit errors, a weighted average of the mean and standard deviation is made using the fit parameters and fit errors as weights from the uncorrelated pull distributions. This is the same technique as was used to determine the systematic error from fluctuations in time. The resulting weighted mean and weighted standard deviation are then used to calculate the systematic error. A summary of the systematic error from each false asymmetry is shown in Table 7.6. The systematic error due to additional factors is chosen as the largest systematic error from Table 7.6.

Systematic error	$\langle \sigma_{\text{systematic}} / \sigma_{\text{statistical}} \rangle$
Two target acceptance estimation	0.19
Target Cell 1	1.20
Target Cell 2	1.11

Table 7.6: Summary of systematic error impacts from false asymmetries changes in time. The maximum systematic error is chosen as the systematic error.

Total Systematics

The total systematic error is determined by adding all systematic errors in quadrature as

$$\left\langle \frac{\sigma_{\text{systematic}}}{\sigma_{\text{statistical}}} \right\rangle = \sqrt{\sum_i^{\text{all systematic}} \left\langle \frac{\sigma_{\text{systematic},i}^2}{\sigma_{\text{statistical}}^2} \right\rangle}, \quad (7.17)$$

where all the systematic effects considered are summarized in Table. 7.7. For reference the total statistical error is $\langle \sigma_{\text{statistical}} \rangle = 0.006$.

Systematic error	$\langle \sigma_{\text{systematic}} / \sigma_{\text{statistical}} \rangle$	$\langle \sigma_{\text{systematic}} \rangle$
Period compatibility	0.16	0.001
Left-Right migration	0.044	0.0003
J/ Ψ purity	0.095	0.0006
Target Polarization	0.05	0.0003
Dilution Factor	0.05	0.0003
Acceptance fluctuation	0.23	0.001
False asymmetry	1.2	0.008
Total	1.24	0.008

Table 7.7: Summary of systematic error impacts to the integrated asymmetry

The integrated left-right asymmetry result and systematic error band is shown in Fig. 7.15 and the kinematic dependencies are shown in Fig. 7.16. Similarly to the left-right asymmetry for the high mass Drell-Yan analysis, the integrated left-right asymmetry is 1 sigma above zero. The asymmetry shows a weak

inverse dependence on x_F indicating the asymmetry could be related to quark distributions in the proton target. This can also be seen in the x_N dependence which is most significant in the highest x_N bin. Although the left-right asymmetry is model independent, it was discussed that the Sivers function could be the cause of for a non-zero left-right asymmetry. A positive left-right asymmetry would be consistent with the sign change hypothesis.

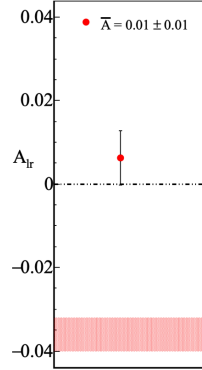


Figure 7.15: The integrated left-right asymmetry from the mass range 2.87-3.38 GeV/c^2 . The systematic error bands are shown in red at the bottom of the plot.

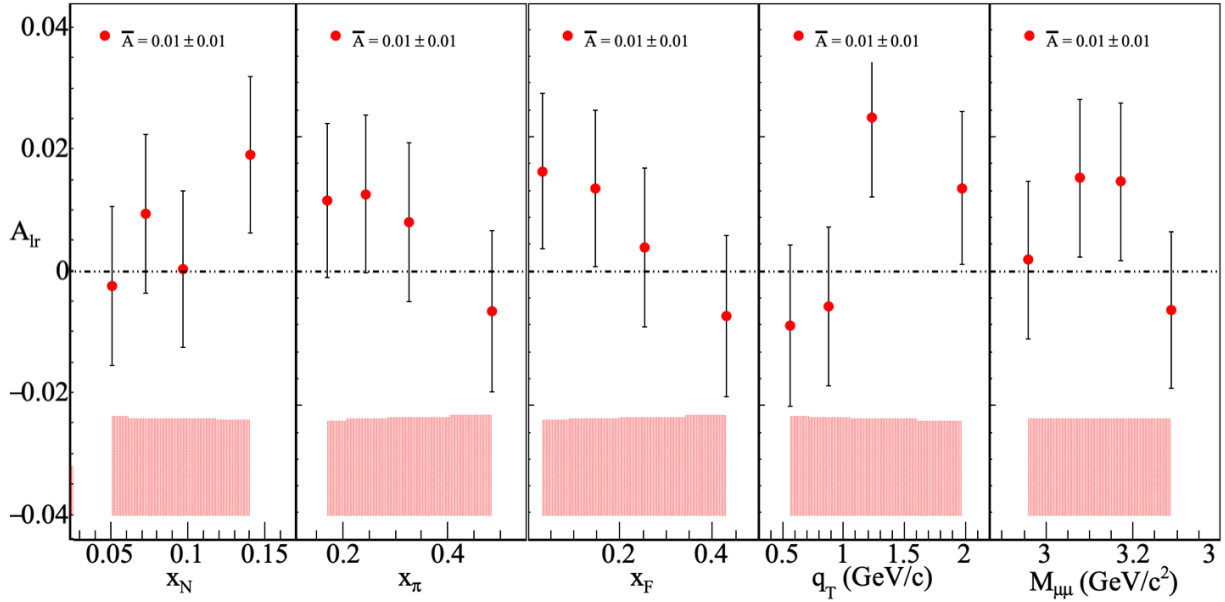


Figure 7.16: The kinematic dependencies of the left-right asymmetry from the mass range 2.87-3.38 GeV/c^2 .

The Anselmino group derived an expression for the A_N asymmetry from J/Ψ production as [\[22\]](#)

$$A_N^{J\Psi} \propto f_{\bar{q}/H_a}(x_a, k_{aT}) \frac{k_{bT}}{M_b} \otimes f_{1T}^{\perp q}(x_b, k_{bT}), \quad (7.18)$$

and a made predictions for the A_N asymmetry as a function of x_N and q_T shown in Fig. 7.17. More details are given in Sec 2.5.4 but their calculation assumed the dominate production of J/ Ψ production is from quark-quark annihilation. Fig. 7.18 shows the results determined at COMPASS for the A_N asymmetry determined by modifying the left-right results in Fig. 7.16. The maximum A_N asymmetry, determined at COMPASS, is less than 0.05 which when comparing to the prediction in Fig. 7.17 is 2 sigma less than the prediction.

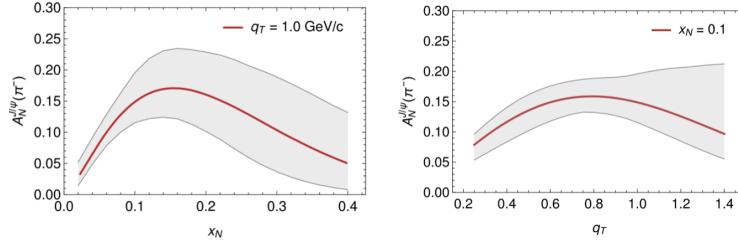


Figure 7.17: Predictions for the analyzing power, A_N , from J/ Ψ production at COMPASS as a function of x_N and q_T . This image was taken from [22].

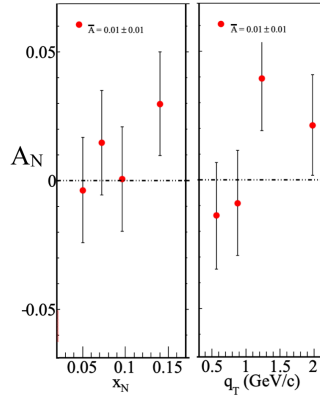


Figure 7.18: The analyzing power at COMPASS determined by modifying the left-right asymmetry as a function of x_N and q_T to be compared with the predictions in Fig. 7.17.

The incompatibility of the theory prediction, Fig. 7.17 and the results determined at COMPASS, Fig. 7.18, can be due to either a Siver function much lower than expected or gluon-gluon fusion contamination. At the present moment, the Siver's function from gluon-gluon fusion is not well known and therefore could be small or negative. Fig. 7.19 shows results for J/ Ψ production from quark-quark annihilation and gluon-gluon fusion using the color evaporation model [23]. To determine the expected J/ Ψ contribution from gluon-gluon fusion and quark-quark annihilation at COMPASS the results in Fig. 7.19 are weighted with the

COMPASS x_F distribution in the intermediate mass range. The determine ratio of J/Ψ production from quark-quark annihilation to gluon-gluon fusion at COMPASS is 0.8. It is therefore not ruled out that the results in Fig. 7.18 are reduced compared to the predictions in Fig. 7.17 due to gluon-gluon fusion.

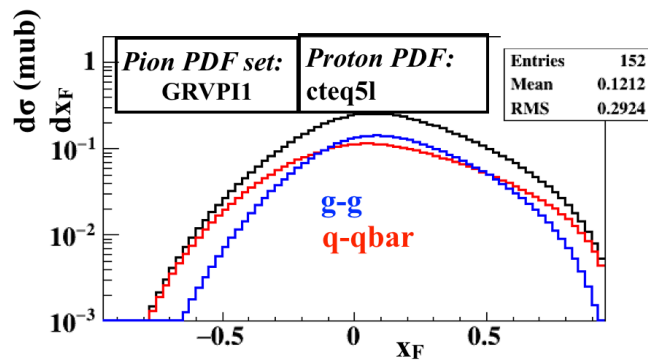


Figure 7.19: J/Ψ production cross-section from gluon-gluon fusion (blue) and quark-quark annihilation (red) and the sum (black) as a function of x_F . This plot is made assuming the color evaporation model [23].

Chapter 8

Conclusion

Mapping out the three dimensional momentum structure of the nucleon is a recent and exciting field. Both theoretical work and experiments have been contributing to the transverse momentum dependent parton distribution functions. This dissertation presents results from dimuon events which originate from a $190 \text{ GeV}/c \pi^-$ on a transversely polarized proton target. The measurements from this thesis expand the knowledge of parton distributions. Specifically the measurements in this thesis add knowledge to the transverse momentum dependent parton distribution functions. The measurements in the high invariant mass region, above $4.3 \text{ GeV}/c^2$, is the worlds first ever transversely polarized Drell-Yan data. The COMPASS spectrometer is unique in that it can perform spin-dependent measurements for Drell-Yan and semi-inclusive deep inelastic scattering in the same kinematic regions.

The analysis techniques in this thesis are constructed to measure azimuthal asymmetry amplitudes where the spectrometer acceptance cancels does not effect the measurement. Several analysis techniques are use and all find the Sivers asymmetry amplitude to be approximately 1 sigma above zero. This result is consistent with the sign change hypothesis between semi-inclusive deep inelastic scattering and Drell-Yan production. At the same time, the statistical error bars are too large to distinguish between the major models of the Sivers function. For this reason the COMPASS collaboration performed another Drell-Yan data taking campaign in 2018 with similar data taking conditions. The results from the 2018 measurement are expected soon.

be approximated as

$$\delta A_{lr,systematic} = \frac{|\alpha - 1|}{2} \frac{1}{|S_T|} + \frac{\delta_{\frac{|\alpha-1|}{2}}}{|S_T|}. \quad (A.7)$$

A.2 Systematic Error From Left-Right Event Migration

Assuming the fraction of events miss-identified is γ and that the amount of miss-identified events reconstructed left equals the amount of outgoing events reconstructed right

$$A_{lr,measure} = \frac{1}{|S_T|} \frac{(l + \frac{\gamma}{2} N_{total}) - (r + \frac{\gamma}{2} N_{total})}{(l + \frac{\gamma}{2} N_{total}) + (r + \frac{\gamma}{2} N_{total})} = \frac{1}{|S_T|} \frac{l - r}{(l + r)(1 + \gamma \frac{N_{total}}{l+r})}, \quad (A.8)$$

where N_{total} is the total events measure, l is the true events measured to the left that should be measured left and r is the number of events measure to the right that should be measured to the right.

Assuming γ is a small percentage, the denominator can be Taylor expanded to give

$$A_{lr,measure} \approx A_{lr} \left(1 - \gamma \frac{N_{total}}{l+r} \right). \quad (A.9)$$

Including $\gamma A_{lr,measure}$ as an additive error and using standard error propagation the systematic error can be approximated as

$$\delta A_{lr,systematic} = \gamma A_{lr,measure} + \gamma \delta A_{lr,measure}. \quad (A.10)$$

A.3 Systematic Error From Event Contamination

Often times the measured counts come from multiple sources where only a measurement from a single source is of interest. As long as the source of interest is dominates the total counts, a left-right asymmetry can still be determined for the source of interest. In this derivation there will be an assumed a signal source with counts N_S and a background source with counts N_{bg} , where the background takes into account all processes that are not of interest. Defining the purity of the signal as

$$p = \frac{N_S}{N_S + N_{bg}}, \quad (A.11)$$

then the left-right asymmetry can be determined as

$$\begin{aligned}
A_{lr} &= \frac{1}{|S_T|} \frac{N_{l,S} + N_{l,bg} - (N_{r,S} + N_{r,bg})}{N_{l,S} + N_{l,bg} + (N_{r,S} + N_{r,bg})} \\
&= \frac{1}{|S_T|} \left\{ \frac{N_{l,S} - N_{r,S}}{N_{l,S} + N_{r,S} + N_{l,bg} + N_{r,bg}} + \frac{N_{l,bg} - N_{r,bg}}{N_{l,bg} + N_{r,bg} + N_{l,S} + N_{r,S}} \right\} \\
&= \frac{1}{|S_T|} \left\{ \frac{N_{l,S} - N_{r,S}}{(N_{l,S} + N_{r,S}) \left(1 + \frac{N_{l,bg} + N_{r,bg}}{N_{l,S} + N_{r,S}}\right)} + \frac{N_{l,bg} - N_{r,bg}}{(N_{l,bg} + N_{r,bg}) \left(1 + \frac{N_{l,S} + N_{r,S}}{N_{l,bg} + N_{r,bg}}\right)} \right\} \\
&= \frac{1}{|S_T|} \left\{ \frac{N_{l,S} - N_{r,S}}{(N_{l,S} + N_{r,S}) \left(\frac{1}{p}\right)} + \frac{N_{l,bg} - N_{r,bg}}{(N_{l,bg} + N_{r,bg}) \left(\frac{p}{1-p}\right)} \right\} \\
&= pA_{lr,S} + \frac{1-p}{p}A_{lr,bg}.
\end{aligned} \tag{A.12}$$

This means that by measuring the purity, p , and the left-right asymmetry, A_{lr} , the left-right asymmetry from the signal, $A_{lr,S}$, can be determined as

$$A_{lr,S} = \frac{1}{p}A_{lr} - \frac{1-p}{p^2}A_{lr,bg}. \tag{A.13}$$

Assuming a purity above 90% and a background left-right asymmetry, $A_{lr,bg}$, of 5%

$$A_{lr,S} = 1.11A_{lr} - 0.123(0.05) = 1.11A_{lr} - 0.006 \approx 1.11A_{lr}. \tag{A.14}$$

The systematic error from a purity less than 1 can be determined as

$$\begin{aligned}
A_{lr,S} &= \frac{1}{p}A_{lr} = A_{lr} + \frac{1-p}{p}A_{lr} \\
\Rightarrow \sigma_{A_{lr,S}}^2 &= \sigma_{A_{lr}}^2 + \frac{(1-p)^2}{p^2}\sigma_{A_{lr}}^2 \\
\Rightarrow \sigma_{systematic}^2/\sigma_{statistic}^2 &= \frac{(1-p)^2}{p^2}.
\end{aligned} \tag{A.15}$$

References

- [1] M. Tanabashi et al. Review of Particle Physics. *Phys. Rev.*, D98(3):030001, 2018. doi: 10.1103/PhysRevD.98.030001.
- [2] Alessandro Bacchetta, Markus Diehl, Klaus Goeke, Andreas Metz, Piet J. Mulders, and Marc Schlegel. Semi-inclusive deep inelastic scattering at small transverse momentum. *JHEP*, 02:093, 2007. doi: 10.1088/1126-6708/2007/02/093.
- [3] M. Alekseev et al. Collins and Sivers asymmetries for pions and kaons in muon-deuteron DIS. *Phys. Lett.*, B673:127–135, 2009. doi: 10.1016/j.physletb.2009.01.060.
- [4] A. Airapetian et al. Observation of the Naive-T-odd Sivers Effect in Deep-Inelastic Scattering. *Phys. Rev. Lett.*, 103:152002, 2009. doi: 10.1103/PhysRevLett.103.152002.
- [5] M. Anselmino, M. Boglione, and S. Melis. Strategy towards the extraction of the sivers function with transverse momentum dependent evolution. *Phys. Rev. D*, 86:014028, Jul 2012. doi: 10.1103/PhysRevD.86.014028. URL <https://link.aps.org/doi/10.1103/PhysRevD.86.014028>.
- [6] C. Adolph et al. Measurement of azimuthal hadron asymmetries in semi-inclusive deep inelastic scattering off unpolarised nucleons. *Nucl. Phys.*, B886:1046–1077, 2014. doi: 10.1016/j.nuclphysb.2014.07.019.
- [7] M. Anselmino, M. Boglione, U. D’Alesio, S. Melis, F. Murgia, and A. Prokudin. Simultaneous extraction of transversity and collins functions from new semi-inclusive deep inelastic scattering and e^+e^- data. *Phys. Rev. D*, 87:094019, May 2013. doi: 10.1103/PhysRevD.87.094019. URL <https://link.aps.org/doi/10.1103/PhysRevD.87.094019>.
- [8] Miguel G. Echevarria, Ahmad Idilbi, Zhong-Bo Kang, and Ivan Vitev. Qcd evolution of the sivers asymmetry. *Phys. Rev. D*, 89:074013, Apr 2014. doi: 10.1103/PhysRevD.89.074013. URL <https://link.aps.org/doi/10.1103/PhysRevD.89.074013>.
- [9] Zhong-Bo Kang and Jian-Wei Qiu. Testing the time-reversal modified universality of the sivers function. *Phys. Rev. Lett.*, 103:172001, Oct 2009. doi: 10.1103/PhysRevLett.103.172001. URL <https://link.aps.org/doi/10.1103/PhysRevLett.103.172001>.
- [10] L. et. al. Adamczyk. Measurement of the transverse single-spin asymmetry in $p^\uparrow + p \rightarrow W^\pm/Z^0$ at rhic. *Phys. Rev. Lett.*, 116:132301, Apr 2016. doi: 10.1103/PhysRevLett.116.132301. URL <https://link.aps.org/doi/10.1103/PhysRevLett.116.132301>.
- [11] R. D. Klem, J. E. Bowers, H. W. Courant, H. Kagan, M. L. Marshak, E. A. Peterson, K. Ruddick, W. H. Dragoset, and J. B. Roberts. Measurement of asymmetries of inclusive pion production in proton-proton interactions at 6 and 11.8 gev/c. *Phys. Rev. Lett.*, 36:929–931, Apr 1976. doi: 10.1103/PhysRevLett.36.929. URL <https://link.aps.org/doi/10.1103/PhysRevLett.36.929>.
- [12] Allgower et. al. Measurement of analyzing powers of π^+ and π^- produced on a hydrogen and a carbon target with a 22 – GeV/c incident polarized proton beam. *Phys. Rev. D*, 65:092008, May 2002. doi: 10.1103/PhysRevD.65.092008. URL <https://link.aps.org/doi/10.1103/PhysRevD.65.092008>.

- [13] D.L. Adams et. al. Comparison of spin asymmetries and cross sections in 0 production by 200 gev polarized antiprotons and protons. *Physics Letters B*, 261(1):201 – 206, 1991. ISSN 0370-2693. doi: [https://doi.org/10.1016/0370-2693\(91\)91351-U](https://doi.org/10.1016/0370-2693(91)91351-U). URL <http://www.sciencedirect.com/science/article/pii/037026939191351U>.
- [14] D.L. Adams et. al. Analyzing power in inclusive + and production at high xf with a 200 gev polarized proton beam. *Physics Letters B*, 264(3):462 – 466, 1991. ISSN 0370-2693. doi: [https://doi.org/10.1016/0370-2693\(91\)90378-4](https://doi.org/10.1016/0370-2693(91)90378-4). URL <http://www.sciencedirect.com/science/article/pii/0370269391903784>.
- [15] Arsene et. al. Single-transverse-spin asymmetries of identified charged hadrons in polarized pp collisions at $\sqrt{s} = 62.4$ GeV. *Phys. Rev. Lett.*, 101:042001, Jul 2008. doi: 10.1103/PhysRevLett.101.042001. URL <https://link.aps.org/doi/10.1103/PhysRevLett.101.042001>.
- [16] Ran Bi. Simulation of Properties of COMPASS Drift-Chamber Prototypes. DNP, 2013.
- [17] IhnJea Choi. DESY Test-Beam Measurement with COMPASS Drift Chamber Prototypes. DNP, 2013.
- [18] M. Aghasyan et al. First measurement of transverse-spin-dependent azimuthal asymmetries in the Drell-Yan process. *Phys. Rev. Lett.*, 119(11):112002, 2017. doi: 10.1103/PhysRevLett.119.112002.
- [19] M. Anselmino, M. Boglione, U. D’Alesio, F. Murgia, and A. Prokudin. Study of the sign change of the Sivers function from STAR Collaboration W/Z production data. *JHEP*, 04:046, 2017. doi: 10.1007/JHEP04(2017)046.
- [20] Miguel G. Echevarria, Ahmad Idilbi, Zhong-Bo Kang, and Ivan Vitev. QCD Evolution of the Sivers Asymmetry. *Phys. Rev.*, D89:074013, 2014. doi: 10.1103/PhysRevD.89.074013.
- [21] Peng Sun and Feng Yuan. Transverse momentum dependent evolution: Matching semi-inclusive deep inelastic scattering processes to Drell-Yan and W/Z boson production. *Phys. Rev.*, D88(11):114012, 2013. doi: 10.1103/PhysRevD.88.114012.
- [22] M. Anselmino, V. Barone, and M. Boglione. The Sivers asymmetry in DrellYan production at the J/Ψ peak at COMPASS. *Phys. Lett.*, B770:302–306, 2017. doi: 10.1016/j.physletb.2017.04.074.
- [23] R. Vogt. J/ψ production and suppression. *Physics Reports*, 310(4):197 – 260, 1999. ISSN 0370-1573. doi: [https://doi.org/10.1016/S0370-1573\(98\)00074-X](https://doi.org/10.1016/S0370-1573(98)00074-X). URL <http://www.sciencedirect.com/science/article/pii/S037015739800074X>.
- [24] E. Rutherford. The scattering of alpha and beta particles by matter and the structure of the atom. *Phil. Mag. Ser.6*, 21:669–688, 1911. doi: 10.1080/14786440508637080.
- [25] Murray Gell-Mann. A Schematic Model of Baryons and Mesons. *Phys. Lett.*, 8:214–215, 1964. doi: 10.1016/S0031-9163(64)92001-3.
- [26] G. Zweig. An SU(3) model for strong interaction symmetry and its breaking. Version 2. In D.B. Lichtenberg and Simon Peter Rosen, editors, *DEVELOPMENTS IN THE QUARK THEORY OF HADRONS. VOL. 1. 1964 - 1978*, pages 22–101. 1964.
- [27] Richard P. Feynman. Very high-energy collisions of hadrons. *Phys. Rev. Lett.*, 23:1415–1417, Dec 1969. doi: 10.1103/PhysRevLett.23.1415. URL <https://link.aps.org/doi/10.1103/PhysRevLett.23.1415>.
- [28] Dennis W. Sivers. Single Spin Production Asymmetries from the Hard Scattering of Point-Like Constituents. *Phys. Rev.*, D41:83, 1990. doi: 10.1103/PhysRevD.41.83.
- [29] Vincenzo Barone, Alessandro Drago, and Philip G. Ratcliffe. Transverse polarisation of quarks in hadrons. *Phys. Rept.*, 359:1–168, 2002. doi: 10.1016/S0370-1573(01)00051-5.

- [30] Elliott D. Bloom et al. High-Energy Inelastic e p Scattering at 6-Degrees and 10-Degrees. *Phys. Rev. Lett.*, 23:930–934, 1969. doi: 10.1103/PhysRevLett.23.930.
- [31] Martin Breidenbach, Jerome I. Friedman, Henry W. Kendall, Elliott D. Bloom, D. H. Coward, H. C. DeStaebler, J. Drees, Luke W. Mo, and Richard E. Taylor. Observed Behavior of Highly Inelastic electron-Proton Scattering. *Phys. Rev. Lett.*, 23:935–939, 1969. doi: 10.1103/PhysRevLett.23.935.
- [32] J. D. Bjorken and Emmanuel A. Paschos. Inelastic Electron Proton and gamma Proton Scattering, and the Structure of the Nucleon. *Phys. Rev.*, 185:1975–1982, 1969. doi: 10.1103/PhysRev.185.1975.
- [33] P. J. Mulders and R. D. Tangerman. The Complete tree level result up to order $1/Q$ for polarized deep inelastic leptonproduction. *Nucl. Phys.*, B461:197–237, 1996. doi: 10.1016/S0550-3213(96)00648-7,10.1016/0550-3213(95)00632-X. [Erratum: Nucl. Phys.B484,538(1997)].
- [34] Daniel Boer and P. J. Mulders. Time reversal odd distribution functions in leptonproduction. *Phys. Rev.*, D57:5780–5786, 1998. doi: 10.1103/PhysRevD.57.5780.
- [35] Juan Rojo et. al. The PDF4lhc report on PDFs and LHC data: results from run i and preparation for run II. *Journal of Physics G: Nuclear and Particle Physics*, 42(10):103103, sep 2015. doi: 10.1088/0954-3899/42/10/103103. URL <https://doi.org/10.1088%2F0954-3899%2F42%2F10%2F103103>.
- [36] B. Adeva et al. The Spin dependent structure function $g(1)(x)$ of the proton from polarized deep inelastic muon scattering. *Phys. Lett.*, B412:414–424, 1997. doi: 10.1016/S0370-2693(97)01106-4.
- [37] A. et al. Airapetian. Flavor decomposition of the sea-quark helicity distributions in the nucleon from semiinclusive deep inelastic scattering. *Phys. Rev. Lett.*, 92:012005, Jan 2004. doi: 10.1103/PhysRevLett.92.012005. URL <https://link.aps.org/doi/10.1103/PhysRevLett.92.012005>.
- [38] I. A. Savin. COMPASS results on the nucleon spin structure. *Nucl. Phys. Proc. Suppl.*, 219-220:94–101, 2011. doi: 10.1016/j.nuclphysb.2011.11.001.
- [39] L. A. Harland-Lang, A. D. Martin, P. Motylinski, and R. S. Thorne. The impact of the final HERA combined data on PDFs obtained from a global fit. *Eur. Phys. J.*, C76(4):186, 2016. doi: 10.1140/epjc/s10052-016-4020-1.
- [40] I. Abt, A. M. Cooper-Sarkar, B. Foster, V. Myronenko, K. Wichmann, and M. Wing. Study of HERA ep data at low Q^2 and low x_{Bj} and the need for higher-twist corrections to standard perturbative QCD fits. *Phys. Rev.*, D94(3):034032, 2016. doi: 10.1103/PhysRevD.94.034032.
- [41] Emanuele R. Nocera, Richard D. Ball, Stefano Forte, Giovanni Ridolfi, and Juan Rojo. A first unbiased global determination of polarized PDFs and their uncertainties. *Nucl. Phys.*, B887:276–308, 2014. doi: 10.1016/j.nuclphysb.2014.08.008.
- [42] M. Hirai and S. Kumano. Determination of gluon polarization from deep inelastic scattering and collider data. *Nucl. Phys.*, B813:106–122, 2009. doi: 10.1016/j.nuclphysb.2008.12.026.
- [43] C. G. Callan and David J. Gross. High-energy electroproduction and the constitution of the electric current. *Phys. Rev. Lett.*, 22:156–159, Jan 1969. doi: 10.1103/PhysRevLett.22.156. URL <https://link.aps.org/doi/10.1103/PhysRevLett.22.156>.
- [44] Stanley J. Brodsky, Dae Sung Hwang, and Ivan Schmidt. Final state interactions and single spin asymmetries in semiinclusive deep inelastic scattering. *Phys. Lett.*, B530:99–107, 2002. doi: 10.1016/S0370-2693(02)01320-5.
- [45] Stanley J. Brodsky, Dae Sung Hwang, and Ivan Schmidt. Initial state interactions and single spin asymmetries in Drell-Yan processes. *Nucl. Phys.*, B642:344–356, 2002. doi: 10.1016/S0550-3213(02)00617-X.
- [46] John C. Collins. Leading twist single transverse-spin asymmetries: Drell-Yan and deep inelastic scattering. *Phys. Lett.*, B536:43–48, 2002. doi: 10.1016/S0370-2693(02)01819-1.

- [47] A. Airapetian et al. Single-spin asymmetries in semi-inclusive deep-inelastic scattering on a transversely polarized hydrogen target. *Phys. Rev. Lett.*, 94:012002, 2005. doi: 10.1103/PhysRevLett.94.012002.
- [48] A. Airapetian et al. Effects of transversity in deep-inelastic scattering by polarized protons. *Phys. Lett.*, B693:11–16, 2010. doi: 10.1016/j.physletb.2010.08.012.
- [49] E. S. Ageev et al. A New measurement of the Collins and Sivers asymmetries on a transversely polarised deuteron target. *Nucl. Phys.*, B765:31–70, 2007. doi: 10.1016/j.nuclphysb.2006.10.027.
- [50] M. G. Alekseev et al. Measurement of the Collins and Sivers asymmetries on transversely polarised protons. *Phys. Lett.*, B692:240–246, 2010. doi: 10.1016/j.physletb.2010.08.001.
- [51] C. Adolph et al. Experimental investigation of transverse spin asymmetries in muon-p SIDIS processes: Collins asymmetries. *Phys. Lett.*, B717:376–382, 2012. doi: 10.1016/j.physletb.2012.09.055.
- [52] C. Adolph et al. Collins and Sivers asymmetries in muonproduction of pions and kaons off transversely polarised protons. *Phys. Lett.*, B744:250–259, 2015. doi: 10.1016/j.physletb.2015.03.056.
- [53] X. et. al. Qian. Single spin asymmetries in charged pion production from semi-inclusive deep inelastic scattering on a transversely polarized ^3He target at $Q^2 = 1.4 - -2.7 \text{ geV}^2$. *Phys. Rev. Lett.*, 107:072003, Aug 2011. doi: 10.1103/PhysRevLett.107.072003. URL <https://link.aps.org/doi/10.1103/PhysRevLett.107.072003>.
- [54] Kazuo Abe et al. Measurement of azimuthal asymmetries in inclusive production of hadron pairs in e^+e^- annihilation at Belle. *Phys. Rev. Lett.*, 96:232002, 2006. doi: 10.1103/PhysRevLett.96.232002.
- [55] R. Seidl et al. Measurement of Azimuthal Asymmetries in Inclusive Production of Hadron Pairs in e^+e^- Annihilation at $\sqrt{s} = 10.58\text{-GeV}$. *Phys. Rev.*, D78:032011, 2008. doi: 10.1103/PhysRevD.78.032011,10.1103/PhysRevD.86.039905. [Erratum: *Phys. Rev.* D86,039905(2012)].
- [56] J. P. Lees et al. Measurement of Collins asymmetries in inclusive production of charged pion pairs in e^+e^- annihilation at BABAR. *Phys. Rev.*, D90(5):052003, 2014. doi: 10.1103/PhysRevD.90.052003.
- [57] S. Arnold, A. Metz, and M. Schlegel. Dilepton production from polarized hadron hadron collisions. *Phys. Rev.*, D79:034005, 2009. doi: 10.1103/PhysRevD.79.034005.
- [58] A. Kotzinian. Description of polarized $\pi^- + N$ Drell-Yan processes, 2010. URL http://wwwcompass.cern.ch/compass/notes_public/2010-2.pdf.
- [59] A. M. Kotzinian and P. J. Mulders. Longitudinal quark polarization in transversely polarized nucleons. *Phys. Rev.*, D54:1229–1232, 1996. doi: 10.1103/PhysRevD.54.1229.
- [60] A. M. Kotzinian and P. J. Mulders. Probing transverse quark polarization via azimuthal asymmetries in leptonproduction. *Phys. Lett.*, B406:373–380, 1997. doi: 10.1016/S0370-2693(97)00708-9.
- [61] A. V. Efremov, K. Goeke, S. Menzel, A. Metz, and P. Schweitzer. Sivers effect in semi-inclusive DIS and in the Drell-Yan process. *Phys. Lett.*, B612:233–244, 2005. doi: 10.1016/j.physletb.2005.03.010.
- [62] A. N. Sissakian, O. Yu. Shevchenko, A. P. Nagaytsev, and O. N. Ivanov. Direct extraction of transversity and its accompanying T-odd distribution from the unpolarized and single-polarized Drell-Yan process. *Phys. Rev.*, D72:054027, 2005. doi: 10.1103/PhysRevD.72.054027.
- [63] A. Sissakian, O. Shevchenko, A. Nagaytsev, O. Denisov, and O. Ivanov. Transversity and its accompanying T-odd distribution from Drell-Yan processes with pion-proton collisions. *Eur. Phys. J.*, C46:147–150, 2006. doi: 10.1140/epjc/s2006-02490-1.
- [64] Zhengxian Wang, Xiaoyu Wang, and Zhun Lu. Boer-Mulders function of pion meson and q_T -weighted $\cos 2\phi$ asymmetry in the unpolarized $\pi^- p$ Drell-Yan at COMPASS. *Phys. Rev.*, D95(9):094004, 2017. doi: 10.1103/PhysRevD.95.094004.

- [65] M. Anselmino, V. Barone, A. Drago, and N. N. Nikolaev. Accessing transversity via J/ψ production in polarized p vector anti-p vector interactions. *Phys. Lett.*, B594:97–104, 2004. doi: 10.1016/j.physletb.2004.05.029.
- [66] V. Barone, Zhun Lu, and Bo-Qiang Ma. The $\cos^2\phi$ asymmetry of drell-yan and j/ψ production in unpolarized pp scattering. *The European Physical Journal C*, 49(4):967–971, Mar 2007. ISSN 1434-6052. doi: 10.1140/epjc/s10052-006-0174-6. URL <https://doi.org/10.1140/epjc/s10052-006-0174-6>.
- [67] A. Sissakian, O. Shevchenko, A. Nagaytsev, and O. Ivanov. Transversity and T-odd PDFs from Drell-Yan processes with p p, p D and D D collisions. *Eur. Phys. J.*, C59:659–673, 2009. doi: 10.1140/epjc/s10052-008-0806-0.
- [68] P. Abbon et al. The COMPASS experiment at CERN. *Nucl. Instrum. Meth.*, A577:455–518, 2007. doi: 10.1016/j.nima.2007.03.026.
- [69] A. Abragam and M. Goldman. Principles of dynamic nuclear polarisation. *Reports on Progress in Physics*, 41:395–467, 1978. doi: 10.1103/PhysRevD.16.2219.
- [70] Radja Boughezal, John M. Campbell, R. Keith Ellis, Christfried Focke, Walter Giele, Xiaohui Liu, Frank Petriello, and Ciaran Williams. Color singlet production at NNLO in MCFM. *Eur. Phys. J.*, C77(1):7, 2017. doi: 10.1140/epjc/s10052-016-4558-y.
- [71] V. Yu. Aleksakhin, Y. Bedfer, S. Gerasimov, and A. Yu. Korzenev. Geometrical event reconstruction in the COMPASS experiment. *Phys. Part. Nucl. Lett.*, 4:350–362, 2007. doi: 10.1134/S1547477107040103. [Pisma Fiz. Elem. Chast. Atom. Yadra2007,no.4,588(2007)].
- [72] R. Fruhwirth. Application of Kalman filtering to track and vertex fitting. *Nucl. Instrum. Meth.*, A262:444–450, 1987. doi: 10.1016/0168-9002(87)90887-4.
- [73] Torbjørn Sjöstrand, Stefan Ask, Jesper R. Christiansen, Richard Corke, Nishita Desai, Philip Ilten, Stephen Mrenna, Stefan Prestel, Christine O. Rasmussen, and Peter Z. Skands. An Introduction to PYTHIA 8.2. *Comput. Phys. Commun.*, 191:159–177, 2015. doi: 10.1016/j.cpc.2015.01.024.
- [74] F Gautheron et al. COMPASS-II Proposal. 2010.
- [75] C. Quintans. LAS Reconstruction Efficiency - DC05/ST03. COMPASS DY, March, 12 2014.
- [76] C. Quintans. LAS Reconstruction Efficiency without DC05/ST03. COMPASS DY, March, 28 2014.
- [77] R. Veenhof. Garfield - simulation of gaseous detectors. <http://cern.ch/garfield>.
- [78] H. Pereira and J. M. Le Goff. Compass Spectrometer Alignment.
- [79] Volker Blobel and Claus Kleinwort. A New method for the high precision alignment of track detectors. In *Advanced Statistical Techniques in Particle Physics. Proceedings, Conference, Durham, UK, March 18-22, 2002*, pages URL–STR(9), 2002. URL <http://www.ipp.dur.ac.uk/Workshops/02/statistics/proceedings//blobel1.pdf>.
- [80] Jan Matousek. *Nucleon spin structure studies in Drell-Yan process at COMPASS*. PhD thesis, University of Trieste, April 2018.
- [81] S. Agostinelli et al. Geant4a simulation toolkit. *Nuclear Instruments and Methods in Physics Research Section A: Accelerators, Spectrometers, Detectors and Associated Equipment*, 506(3):250 – 303, 2003. ISSN 0168-9002. doi: [https://doi.org/10.1016/S0168-9002\(03\)01368-8](https://doi.org/10.1016/S0168-9002(03)01368-8). URL <http://www.sciencedirect.com/science/article/pii/S0168900203013688>.
- [82] T. Szameitat. *New Geant4-based Monte Carlo Software for the COMPASS-II Experiment at CERN*. PhD thesis, Albert-Ludwigs-Universität Freiburg, 2017.